remote sensing

MDPI

Article

High-Resolution Nearshore Sea Surface Temperature from Calibrated Landsat Brightness Data

William H. Speiser [1,2,*] and **John L. Largier** [1,2,3]

[1] Hydrologic Sciences Graduate Group, University of California Davis, Davis, CA 95616, USA; jlargier@ucdavis.edu
[2] Bodega Marine Laboratory, Coastal and Marine Sciences Institute, University of California Davis, Bodega Bay, CA 94923, USA
[3] Department of Environmental Science and Policy, University of California Davis, Davis, CA 95616, USA
* Correspondence: whspeiser@ucdavis.edu

Abstract: Understanding and monitoring nearshore environments is essential, given that these fine-scaled ecosystems are integral to human well-being. While satellites offer an opportunity to gain synchronous and spatially extensive data of coastal areas, off-the-shelf calibrated satellite sea surface temperature (SST) measurements have only been available at coarse resolutions of 1 km or larger. In this study, we develop a novel methodology to create a simple linear equation to calibrate fine-scale Landsat thermal infrared radiation brightness temperatures (calibrated for land sensing) to derive SST at a resolution of 100 m. The constants of this equation are derived from correlations of coincident MODIS SST and Landsat data, which we filter to find optimal pairs. Validation against in situ sensor data at varying distances from the shore in Northern California shows that our SST estimates are more accurate than prior off-the-shelf Landsat data calibrated for land surfaces. These fine-scale SST estimates also demonstrate superior accuracy compared with coincident MODIS SST estimates. The root mean square error for our minimally filtered dataset (n = 557 images) ranges from 0.76 to 1.20 °C with correlation coefficients from r = 0.73 to 0.92, and for our optimal dataset (n = 229 images), the error is from 0.62 to 0.98 °C with correlations from r = 0.83 to 0.92. Potential error sources related to stratification and seasonality are examined and we conclude that Landsat data represent skin temperatures with an error between 0.62 and 0.73 °C. We discuss the utility of our methodology for enhancing coastal monitoring efforts and capturing previously unseen spatial complexity. Testing the calibration methodology on Landsat images before and after the temporal bounds of accurate MODIS SST measurements shows successful calibration with lower errors than the off-the-shelf, land-calibrated Landsat product, extending the applicability of our approach. This new approach for obtaining high-resolution SST data in nearshore waters may be applied to other upwelling regions globally, contributing to improved coastal monitoring, management, and research.

Keywords: Landsat; MODIS; sea surface temperature; nearshore oceanography; coastal upwelling

check for updates

Citation: Speiser, W.H.; Largier, J.L. High-Resolution Nearshore Sea Surface Temperature from Calibrated Landsat Brightness Data. *Remote Sens.* **2024**, *16*, 4477. https://doi.org/10.3390/rs16234477

Academic Editor: Biao Zhang

Received: 4 October 2024
Revised: 25 November 2024
Accepted: 26 November 2024
Published: 28 November 2024

1. Introduction

The ocean is vast and most direct human interaction occurs in nearshore waters, which also host the most productive ecosystems [1]. There are relatively few data from waters within a few kilometers of land, which is a major oversight given the importance of these waters for ecosystems and humans [2], and it is often assumed that waters are quite uniform and like those further offshore over the continental shelf. While satellites offer an opportunity to gain synchronous and spatially extensive data of these understudied areas, there are no publicly available platforms that provide reliable surface properties at a spatial scale sufficient to resolve primary nearshore flow features and dynamics. Specifically, sea surface temperature (SST) has historically been available at a scale of 1 km or larger and these data are notorious for poor reliability within a pixel of the shoreline due to contamination [3–5]. Newer satellites, like GCOM-C, launched on 23 December 2017, offer higher-resolution SST at 0.5 km with a 2–3-day overpass frequency. However, due to its moderate resolution and recent launch, it likely cannot resolve variable nearshore features. Through the calibration of high-resolution Landsat brightness temperature data with concurrent, long-operating, low-resolution MODIS SST data, we developed a new method and dataset that effectively resolves fine-scale SST patterns in nearshore waters with high fidelity.

Nearshore water circulation differs markedly from offshore regions due to the proximity and shape of the shoreline and shoals. Phenomena include wave-driven flows [6,7], large and small river outflow plumes [8–10], tidal jets [11,12], internal wave shoaling [13], the coastal boundary layer [14], and small-scale wind effects [15]. These flow features account for complex patterns in water properties, including temperature and salinity as well as biogeochemical (oxygen, pH, pCO_2, NO_3) and biological (phytoplankton, meroplankton, and pathogenic microbes) parameters. At times, these patterns are made visible by a concurrent turbidity or a water color signal, which can be detected by high-resolution optical satellite imagery [10]. However, few reliable methods exist for obtaining satellite-based data on sea surface temperature at sufficient spatial resolution, despite the ubiquity of thermal patterns in nearshore waters. While there is an increasing number of studies based on numerical experiments and in situ field sensors [16], their scope is generally limited by scale and the full complexity of multi-scale nearshore circulation processes remains unresolved [17].

The Landsat series of satellites operated by the United States Geological Survey (USGS) contains onboard thermal infrared radiation (TIR) sensors with a spatial resolution (60–120 m) fine enough to resolve the primary nearshore circulation features with a sub-kilometer scale. However, these satellites lack atmospheric self-correction capabilities owing to a limited number of TIR range bands, which precludes the conversion of TIR brightness values to sea surface temperature values without external empirical calibration.

Prior studies have used several methods to extract SST information from Landsat TIR data. Some studies have used off-the-shelf Landsat Level 2 brightness temperature data, calibrated by the USGS for land surfaces [4,18–21]. These studies often look at trends or spatial gradients rather than actual SST values because of the limited accuracy of Landsat Level 2 brightness temperature data for ocean sensing [19,20]. Other software packages like ACOLITE [22] derive surface temperatures by converting atmospherically corrected surface radiance using Planck's Law (see Section 2.4) enhanced by radiative transfer models; however, these methods rely on accessing abundant coincidental data, which often complicates atmospheric correction. Other studies have calibrated brightness data with in situ/buoy measurements and are limited to local settings [23–26]. Studies solely using Landsat data often note issues with accuracy in sensing nearshore SST [27]. While prior studies have explored the correlation of Landsat data with coincident satellite data from geostationary satellites [28] or polar orbiting satellites like MODIS and AHVRR [29–33], these studies have been limited to less than 50 images, which is insufficient for capturing nearshore variability and does not aggregate statistics to form generalized calibration constants. That methodology also depends on other satellite missions as well as their continuation for future calibrations, which is a problem as satellites eventually age past their expected mission lifetimes and data quality degrades. Notably, MODIS is now past its expected mission lifetime and has been shown to have unreliable data quality for SST products past 2023 [34]. Furthermore, this methodology requires manual inspection and selection of data to avoid any sources of heterogeneity within images, which is arduous and limits the dataset size.

In this paper, we calibrate an extensive dataset of several hundred Landsat 7–9 images using coincidental MODIS SST (M_{SST}) data captured prior to 2023 for coastal waters off northern California. Our initial approach is to create a unique calibration equation for each image, and our final product is a single equation obtained from median values of the single-image calibrations that can be applied to images outside of the sample set without having to conduct individual image calibrations. We test this sample calibrated Landsat SST data (as well as Landsat SST data before and after MODIS operational dates) against in situ temperature measurements from five locations, showing the superior utility of the aggregate calibration equation for use in SST remote sensing, which also outperforms the use of the off-the-shelf USGS land surface temperature measurements and MODIS. The resultant high-resolution SST data will greatly advance the study of nearshore flow features, hydrodynamic processes, and habitat patterns.

2. Methods

This study investigates the efficacy of Landsat surface brightness temperatures calibrated with MODIS Terra sea surface temperature data to produce high-spatial-resolution SST measurements. We test these calibrations between individual images and use aggregated calibration equations to create a generalized calibration equation made from constants derived from statistics gathered from individual image calibrations. These estimated SST data are validated using in situ monitoring data taken throughout the study region, captured at the same time as the satellite overpass.

2.1. Study Site

Data used for this study are captured within Landsat Worldwide Reference System (WRS) location path 45, row 33, spanning latitudinal coordinates from 37.90 to 39.95 (Figure 1). This area extends across a coastal upwelling region from the mouth of San Francisco Bay northward to Cape Mendocino, covering a geomorphologically and hydrodynamically diverse coastline that contributes to the nearshore temperature structure through phenomena such as runoff from ephemeral streams and small mountain river systems, tidal jets, and flow separation at headlands. This region has a typical "Mediterranean" climate, with seasonal precipitation in winter months, when rainstorms lead to pulses of freshwater runoff and associated river plumes (e.g., off the Russian River, Gualala River, Big River, Noyo River, Albion River, and Navarro River (Figure 1)). During high river flow, buoyant low-salinity plumes from these rivers extend tens of kilometers alongshore [10], and in the dry season, river flow decreases and the estuaries can be closed off from the ocean by sand berms [35], precluding surface exchange with the ocean.

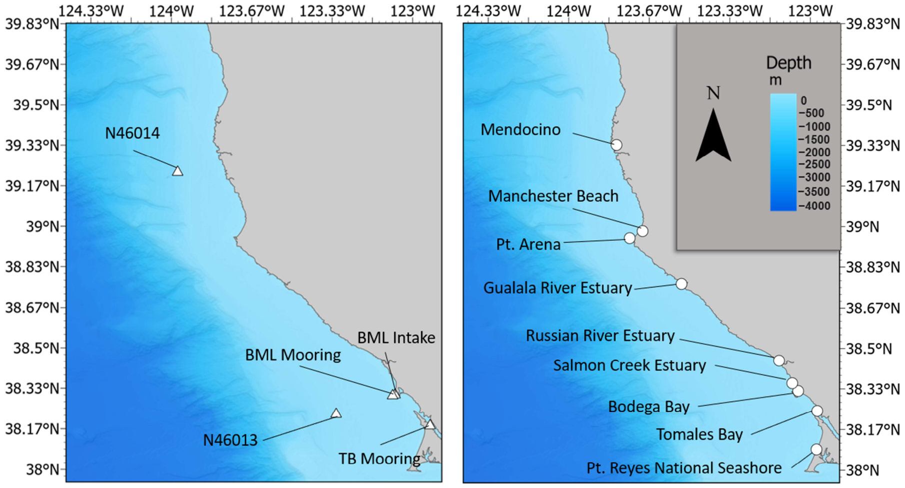

Figure 1. Map of study region in WRS path 45 row 33. (**Left**) Map of in situ validation sites, from north to south: NOAA N46014 (buoy), BOON Intake (seawater intake), BML Mooring (buoy), NOAA N46013 (buoy), and BOON Tomales Bay (buoy). (**Right**) Map of geographical points of interest, from north to south: Mendocino, Manchester Beach, Pt. Arena, Gualala River Estuary, Russian River Estuary, Salmon Creek Beach, Bodega Bay, Tomales Bay, and Pt. Reyes National Seashore. Bathymetric basemap data were accessed from the General Bathymetric Chart of the Ocean (https://www.gebco.net/), with color scaled to depth in meters as shown in the legend.

Wind patterns in the region are also seasonal. From April to June, persistent northerly winds induce upwelling, followed by weaker winds from July to September and more variable winds in the storm season from December to February [36]. Spring upwelling causes nearshore cooling from offshore advection of warmer surface water. The most marked cooling from upwelling occurs in the region south of Pt. Arena and north of the Russian River [37,38].

2.2. Satellite Data

All Landsat 5–9 Level 2 (L2) thermal infrared radiation Landsat Brightness Temperature B_t data within the World Reference System (WRS) scene location at Path 45 Row 33 were collected from Google Earth Engine [39], extending from March 1984 to May 2023. For the Landsat L2 product, the USGS has calibrated Landsat surface radiance L_s to a brightness temperature B_t for land surface temperatures by applying Planck's equation.

$$B_t = \frac{K_2}{\ln\left(\frac{K_1}{L_s} + 1\right)} \tag{1}$$

where B_t is the brightness temperature, K_1 = (L7: 666.0900; L8: 774.8853; L9: 799.0284), K_2 = (L7: 1282.7100; L8: 1321.0789; L9: 1329.2405), and L_s is surface radiance in W/(m^2 sr µm) [40,41]. These temperature data, in degrees Kelvin, are stored as values scaled by a factor of 0.00341802 and offset by a value of 149 to convert data to integers for more efficient storage. Clouds and cloud shadow detection within these images were performed using the CFMASK algorithm [42]. This algorithm employs decision trees, validated by scene-wide statistics, to accurately label pixels affected by clouds and their shadows. These cloud-affected regions are further delineated based on cloud height and the solar angle, enhancing the precision of cloud and shadow detection. Land features were then masked from each image using the high-resolution NOAA Continually Updated Shoreline Product (NOAA CUSP: https://shoreline.noaa.gov/data/datasheets/cusp.html (accessed on 10 February 2024)). This geospatial land dataset is derived from repositories of LiDAR data and individual shoreline datasets; it estimates continental shorelines on a scale from 1:1000 to 1:24,000.

Landsat 7 (L7), operational since 1999, features Band 6 (10.40–12.50 µm), which is specifically dedicated to collecting TIR readings with a resolution of 60 m. However, L7 encountered a known issue with its scan line corrector (SLC) in 2003, leading to data gaps in its imagery [43]. Despite this, its high-resolution thermal data remain invaluable. L7 has a 16-day revisit cycle and typically overpasses a given location at 10:30 a.m., contributing to the temporal coverage of the study.

Both Landsat 8 (L8) and Landsat 9 (L9) are equipped with two TIR sensors of the same range, but temperature is typically derived with the Band 10 sensor (10.60–11.19 µm) due to its reduced sensitivity to stray light in contrast to the other TIR sensor from the curvature of its lens [31,44]. L8 launched in 2013 and L9 launched in 2021 follow a similar 16-day overpass cycle as L7, also capturing mid-morning data.

To align the resolution disparities among the Landsat satellites, L7 images were resampled from their native 60 m resolution to 100 m using bilinear interpolation, matching the resolution of L8 and L9 images. Out of the 705 images obtained across these missions, 659 images were used, the rest being omitted for having pixel count (n) < 100 pixels or when coincident M_{SST} images had a low/zero pixel count. Statistics on pixel availability are displayed in Figure 2, showing that on average, the most available pixels are captured in April and September, while the least are captured in July and August, perhaps due to coastal fog that is prominent during the summer months in the Northern California region [45,46].

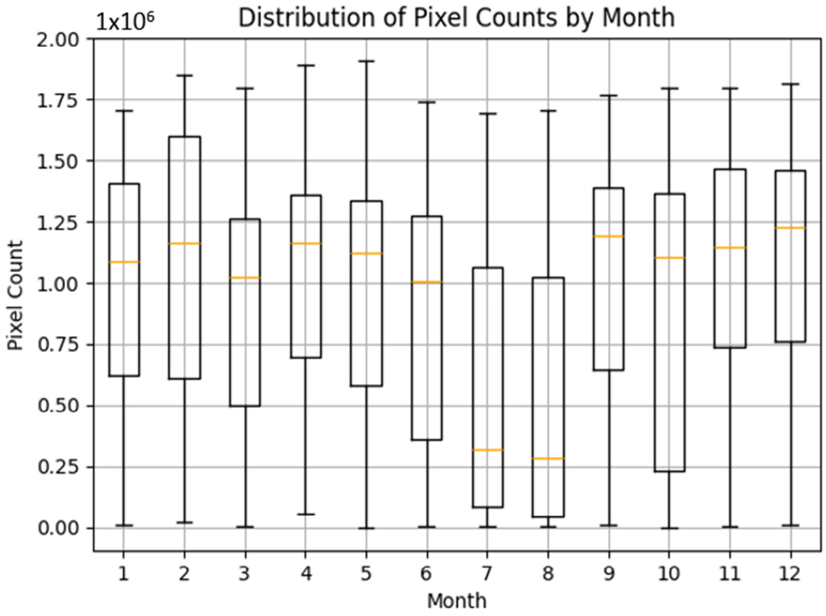

Figure 2. Box and whisker plot of the number of pixels per image by month in the "all" dataset. Box margins are the 25th percentile of data (lower) and 75th percentile of data (upper). The line in the box is the monthly median. Whiskers show minimum and maximum values.

Although Landsat 5 (operational from 1984 to 2013) captures TIR data in a similar spectral range and has a similar overpass window as L7, and it also has data during the timeframe available for this study, it has a spatial resolution of 120 m, which is coarser than the 100 m that we resample images to for this study. Additionally, L5 experienced a gradual shift in its solar zenith angle over time due to changes in orbital altitude [47]. This led to its exclusion from initial data calibrations. Nonetheless, because of its spectral range, L5 data are used in this study as a blind dataset to test the generalizability of calibration constants derived from our methods for dates prior to the launch of MODIS Terra.

We directly downloaded atmospherically corrected and cloud-masked MODIS Terra SST (M_{SST}) datasets from the NASA Ocean Color website (http://oceancolor.gsfc.nasa.gov/, accessed on 2 October 2024). These M_{SST} data, provided at 1 km resolution, are known for their efficacy and accuracy in measuring SST [48]. We specifically chose MODIS Terra over MODIS Aqua as its overpass (typically between 10:30 and 11:30 a.m. local time) overlaps with that of L5, L7, L8, and L9. This ensures minimal temporal discrepancy, ranging from near-instantaneous to a maximum of about two hours, between the image captures of the two satellites. For the data analyzed, the median difference in image capture times on coinciding dates was 27.2 min. MODIS imagery past 2023 is unreliable due to orbital drift; as it exceeded its expected operational time, it has run out of fuel for orbit adjustment [34]. As a result, we only calibrate images from the MODIS mission start date until 1 January 2023.

2.3. Brightness Temperature to Sea Surface Temperature Calibration

In the first step of our method, we calibrate Landsat (L7, L8, and L9) B_t to SST using M_{SST} data from the same date. For each Landsat–MODIS image pair, we calculate Pearson's correlation coefficient r to assess the linear correlation between the SST value of each MODIS pixel and the median value of all Landsat B_t pixels within that MODIS pixel's area. We then exclude any M_{SST}/B_t pairs that deviate by more than one standard deviation ("outliers") and recalculate the correlation. This process is iterated until the correlation coefficient stabilizes or decreases. We then use this best-fit linear equation to convert Landsat B_t data to SST data (Figure 3). To calculate the best-fit linear equation, ordinary least squares (OLS) regression was used.

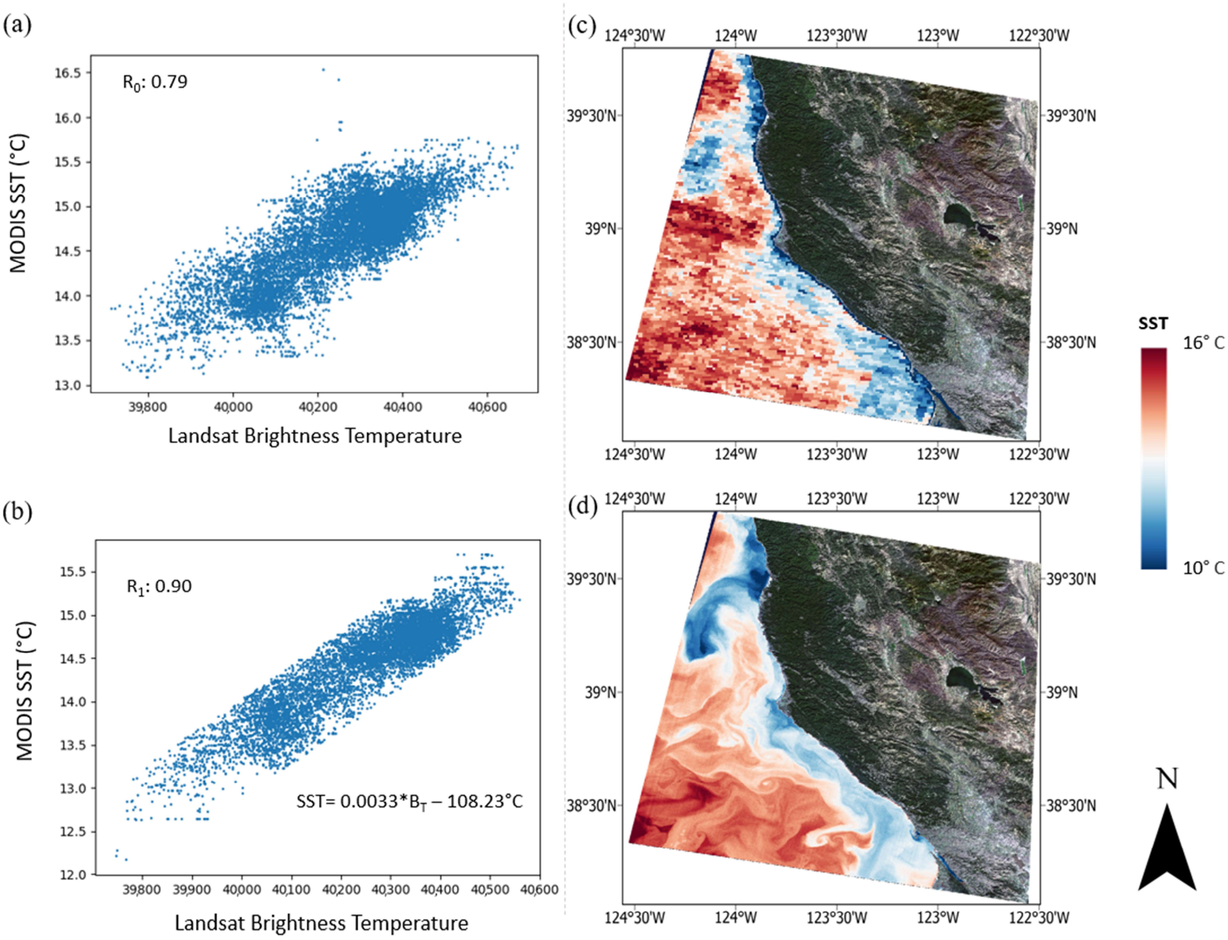

Figure 3. Example of calibration of Landsat B_t to SST using coincidental MODIS Terra SST data from images captured on 7 January 2015 (MODIS at 18:20 LST and Landsat at 18:51 LST). (**a**) Initial correlation between MODIS SST pixels and respective pixel area median Landsat B_t pixel values from 7 January 2015. (**b**) Final correlation after iterative outlier removal as outlined in Section 2.3. (**c**) MODIS Terra SST image from 7 January 2015. (**d**) Estimated Landsat SST obtained by calibrating Landsat B_t values with the best-fit linear equation from panel (**b**).

This first step builds on Thomas et al. (2002) [29] and Snyder et al.'s (2017) [31] work, differing by using the median Landsat pixel value within each MODIS pixel area rather than pairing the nearest Landsat pixel to the nearest MODIS pixel, aiming to reduce pixel heterogeneity and improve accuracy. This calibration step is referred to as "per-image calibration" in this study.

As noted by Snyder et al., 2017 [31], this process assumes that atmospheric conditions are uniform across the Landsat scene and that atmospheric and oceanic conditions do not significantly vary between MODIS and Landsat image captures. Furthermore, as each Landsat scene is captured in scans rather than instantaneously, this method assumes atmospheric and oceanic conditions do not significantly change during image collection; however, scans last only a few seconds. Additionally, this approach assumes that MODIS SST data possess minimal uncertainty and error, enabling their use as the calibration standard for Landsat SST. This assumption implies that any variation in the regression is primarily attributed to the Landsat B_t data.

Using this process, we can categorize images as acceptable or not by examining B_t-M_{SST} correlation strengths. For this study, we considered the image dataset in two groupings, namely an "all data" group and a "selected" (R_0) group. For the "all data" dataset, we use data in which the final r value is above 0.7, thus discarding data that had too many image artifacts to successfully calibrate to SST from B_t. For the "selected" R_0

data, we used Landsat images where the initial r value is above 0.7 prior to iterative outlier removal. This differs from past work, in which images were manually selected through visual inspection. Here, we remove or retain images based on correlative strength, reducing the time spent on data curation and utilizing many more images.

In addition to determining per-image calibrations, we determine a generalized calibration by aggregating per-image calibrations to develop a single linear relationship between SST and Landsat B_t. This approach improves calibrations in general by mitigating the effect of heterogeneity (potential noise from outlier pixels not removed), and it allows for the application to images outside of the original dataset (including times when MODIS data are not available). We aggregate the statistics of the per-image M_{SST}-B_t relationships by finding the median slope (m) and intercept (b) across the R_0 "selected" dataset to obtain

$$\mathrm{SST} = \mathrm{m} * \mathrm{B_t} + \mathrm{b} \tag{2}$$

where SST is the estimated sea surface temperature and B_t is the brightness temperature at a given pixel position. This is the first time such a calibration method utilizing per-image calibration statistics has been employed that the authors are aware of. This "generalized calibration" is a novel approach, and we contrast it with "per-image calibration" approaches.

This generalized equation is applied to all L2 Landsat B_t images in the dataset. It is also tested by applying it to images outside of the dataset without coincident MODIS data (prior or past operational extent). For the latter application, we use L5 data prior to the launch of MODIS Terra and L8 or L9 data after 1 January 2023, when MODIS data are unreliable. We resampled L5 resolution to 100 m using bilinear interpolation prior to calibration to match the resolution of the L7–9 dataset. These test data were then compared with coincidental sensor measurements at specific pixel positions (see Section 2.3 and Table 1).

Table 1. Summary of available in situ sensor data, including coordinates, depth ("D"), distance offshore ("Dist"), sensor type, historical data extent at study time, coordinates of nearest Landsat pixel for validation, count of SST imagery on matching in situ data dates, and correlation/error metrics from comparing in situ data with MODIS SST (M_{SST}), as well as "all data" calibrated Landsat (All), "selected" calibrated Landsat (R0), and uncalibrated Landsat (Bt) data. Correlation (r) and error metrics ($RMSE_{OLS}$, $RMSE_{1:1}$) are from a generalized calibration (Equation (3)). "NA" indicates unavailable data.

Name Coordinate Depth (D) Distance Offshore (Dist)	**Type**	**Extent**	**Pixel**	**Count**	**r**	**$RMSE_{OLS}$**	**$RMSE_{1:1}$**
N46014: 39.225°N, 123.980°W D: 2.0 m Dist: 15.6 km	Buoy	04/1981–05/2023	39.23078°N, 123.97424°W	All: 300 R_0: 147 B_t: 323 M_{SST}: 294	All: 0.83 R_0: 0.91 B_t: 0.75 M_{SST}: 0.70	All: 0.89 R_0: 0.62 B_t: 1.04 M_{SST}:1.13	All: 1.15 R_0: 1.06 B_t: 1.86 M_{SST}: 1.55
N46013: 38.235°N, 123.317°W D: 2.0 m Dist: 23.0 km	Buoy	04/1981–05/2023	38.23544°N, 123.31667°W	All: 385 R_0: 175 B_t: 376 M_{SST}: 376	All: 0.79 R_0: 0.87 B_t: 0.65 M_{SST}: 0.69	All: 1.04 R_0: 0.73 B_t: 1.30 M_{SST}: 1.22	All: 1.25 R_0: 1.17 B_t: 2.00 M_{SST}: 1.53
BML Mooring: 38.312°N, 123.083°W D: 1.0 m Dist: 1.0 km	Buoy	09/2012–05/2023	38.31180°N, 123.08312°W	All: 67 R_0: 40 B_t: 134 M_{SST}: 40	All: 0.92 R_0: 0.92 B_t: 0.87 M_{SST}: 0.87	All: 0.76 R_0: 0.65 B_t: 0.93 M_{SST}: 0.92	All: 0.95 R_0: 1.00 B_t: 1.63 M_{SST}: 1.31
TB Mooring: 38.188°N, 122.928°W D: 1.0 m Dist: 0.34 km	Buoy	05/2013–10/2021	38.18783°N, 122.92771°W	All: 204 R_0: 95 B_t: 220 M_{SST}: NA	All: 0.85 R_0: 0.92 B_t: 0.81 M_{SST} = NA	All: 1.25 R_0: 0.98 B_t: 1.41 M_{SST} = NA	All: 1.56 R_0: 1.42 B_t: 2.53 M_{SST} = NA
BML intake: 38.316°N, 123.070°W D: 2.5–4.5 m tidal Dist: 0 km	Intake	04/1988–05/2023	38.31539°N, 123.07324°W	All: 425 R_0: 188 B_t: 451 M_{SST}: 50	All: 0.73 R_0: 0.83 B_t: 0.62 M_{SST}: 0.80	All: 1.20 R_0: 0.89 B_t: 1.40 M_{SST}: 1.17	All: 1.56 R_0: 1.58 B_t: 2.08 M_{SST}: 1.95

2.4. Data Validation

Landsat SST derived from both per-image calibration and generalized-equation calibration are tested against in situ seawater temperature (T_{insitu}) from sensors deployed on the NOAA National Data Buoy Center buoys N46013 and N46013 (https://www.ndbc.

noaa.gov/, accessed on 10 February 2024), from sensors deployed on buoys in Tomales Bay (TB Mooring) and off Bodega Bay (BML Mooring), and from a sensor deployed on the Bodega Marine Laboratory seawater intake (BML Intake; https://boon.ucdavis.edu/, accessed on 10 February 2024)—see Table 1 and Figure 1. These measurement locations are at varying distances offshore in order to capture variation across marine environments (i.e., offshore, nearshore, at-shore, estuary). Landsat and in situ data were constrained to a temperature range of 5 to 25 °C to eliminate extreme values caused by inaccuracies in sea surface emissivity due to undetected image artifacts (clouds, shadows, and glint).

Hourly averaged in situ data are compared against SST data from the 100 m Landsat pixel at that site. Sensor data at the BML Intake are compared to the pixel nearest to the seawater intake. Sensor temperature data overlap with the MODIS capture time for each date. As all of these in situ measurements are taken at depth (Table 1), a discrepancy is expected between the sub-surface sensor temperature and the SST value, related to the depth of the sensor and the strength of the near-surface stratification [49]. Furthermore, in using in situ buoy measurements to validate the accuracy of these calibrated Landsat SST data, we assume minimal uncertainty and error in these sensors' measurements, treating the use of buoy data as a reliable comparative standard.

To test our calibrations, we use Pearson's r correlation between T_{insitu} and SST at the pixel (Table 1) closest to the buoy, determining the root mean square error RMSE from the 1:1 line ($RMSE_{1:1}$) and from the ordinary least squares (OLS) linear best-fit line ($RMSE_{OLS}$). We also compare sensor measurements with SST estimates from M_{SST} and B_t to benchmark the relative performance of our methodology. We only use M_{SST} images from the same dates in which Landsat imagery is available to make a direct comparison. Landsat B_t data are not filtered by date.

3. Results

3.1. Sea Surface Temperature Calibration

Of the 659 images calibrated for SST from L7 to L9, 557 images are considered as viable for the "all data" dataset. These images went through a median of 6.0 iterations of outlier removal. There was no observable relationship between the number of iterations and the final Pearson's r value. Of those images, 229 images were also in the "selected" R_0 dataset. Correlation values between coincident B_t and M_{SST} values were high from April to September, i.e., during the spring and summer upwelling season in northern California (Figure 4). Variation in OLS best-fit equation constants was low in these seasons (Figures 4 and 5). The lowest slope and smallest intercept values from these OLS best-fit line equations were, respectively, lowest and closest to zero (closer to a 1:1 relation) during this season.

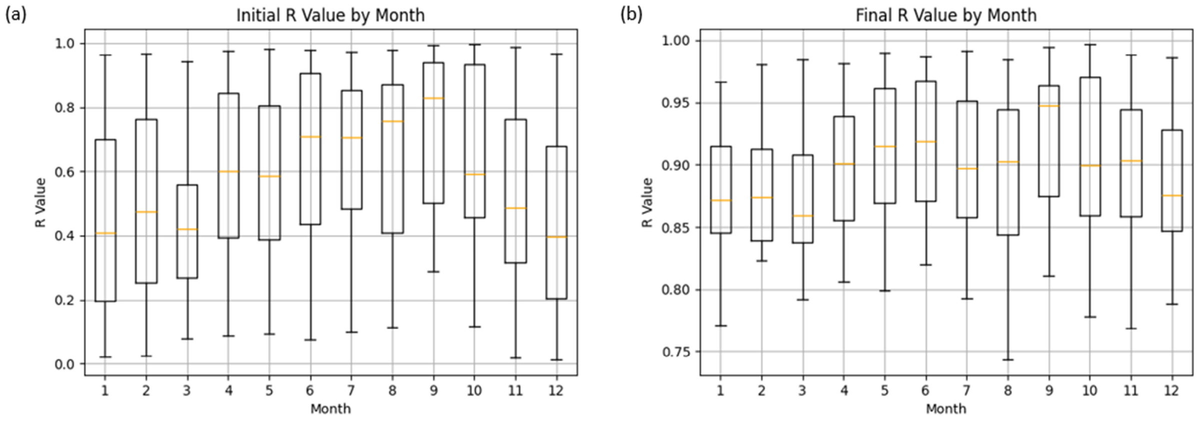

Figure 4. *Cont.*

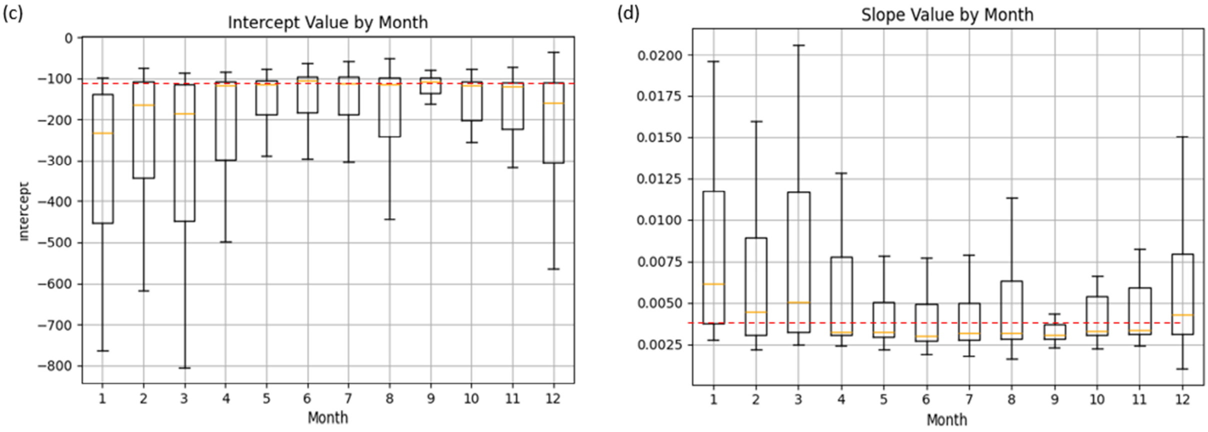

Figure 4. Monthly box and whisker plots from calibration of all data. Box margins are lower 25th percentile of data (lower) and 75th percentile of data (upper). Orange line in box is monthly median. Whiskers show minimum and maximum values. Red dotted line in c. and d. is overall average value. (**a**) Pearson's r correlation values from first iteration of per-pixel comparisons between Landsat B_t and M_{SST}. (**b**) Pearson's r correlation values from final iteration of per-pixel comparisons after iterative outlier removal between Landsat B_t and M_{SST}. (**c**) Intercept values from OLS best-fit linear equations from final iteration comparisons between Landsat B_t and M_{SST}. (**d**) Intercept values from OLS best-fit linear equations from final iteration comparisons between Landsat B_t and M_{SST}.

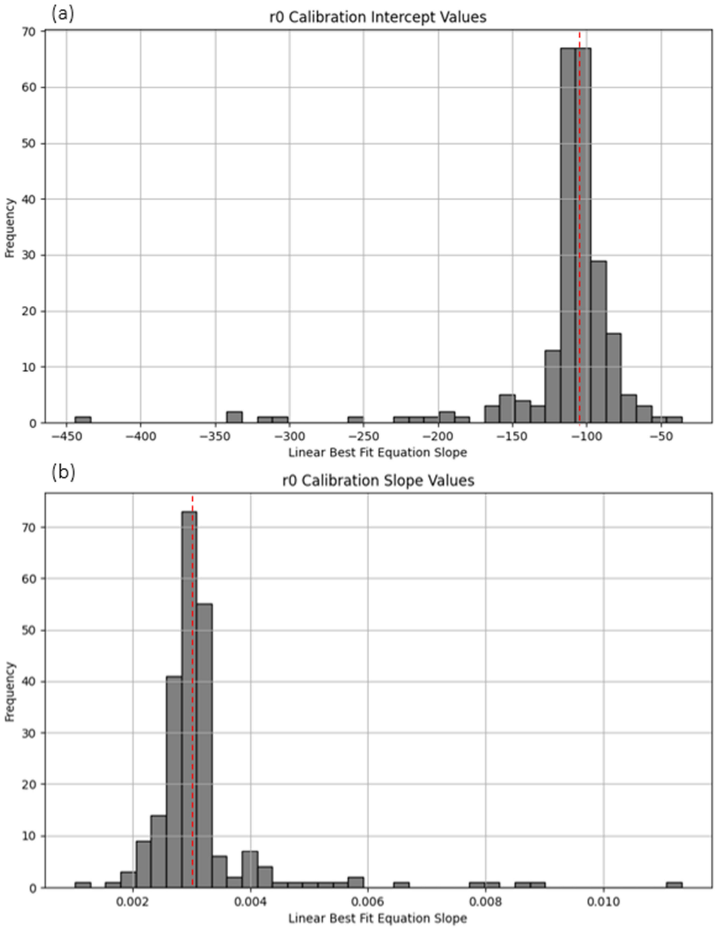

Figure 5. (**a**) Histogram of intercept (b) values from per-image calibrations of R_0 data. (**b**) Histogram of slope (m) values from per-image calibrations of R_0 data. Red lines indicate distribution medians (b = −105.88; m = 0.00297).

The distribution of m and b values from the individual M_{SST}-B_t calibrations within the R_0 dataset are plotted in histograms in Figure 5. From these calibrations, the median of slope values is m = 0.00297 and the median of intercept values is b = 105.879, yielding the "generalized calibration" equation.

$$SST = 0.00297B_t - 105.88^{\circ} \tag{3}$$

A total of 90% of the slope and intercept values fall within 10% of each respective constant value.

3.2. Data Validation Results

To explore the effectiveness of calibrations from per-image analysis, we compare SST values with coincidental in situ measurements at each site, noting variability by site (Figure 6). Within the "all data" group, BML Mooring showed the highest correlation (r = 0.79) and lowest error relative to the 1:1 line ($RMSE_{1:1}$ = 1.49 °C), while N46013 (r = 0.63) had the weakest correlation and TB Mooring had the highest errors ($RMSE_{OLS}$ = 1.77 °C; $RMSE_{1:1}$ = 3.00 °C). Overall, the accuracy of "all data" SST estimates were comparable to B_t and M_{SST} estimates.

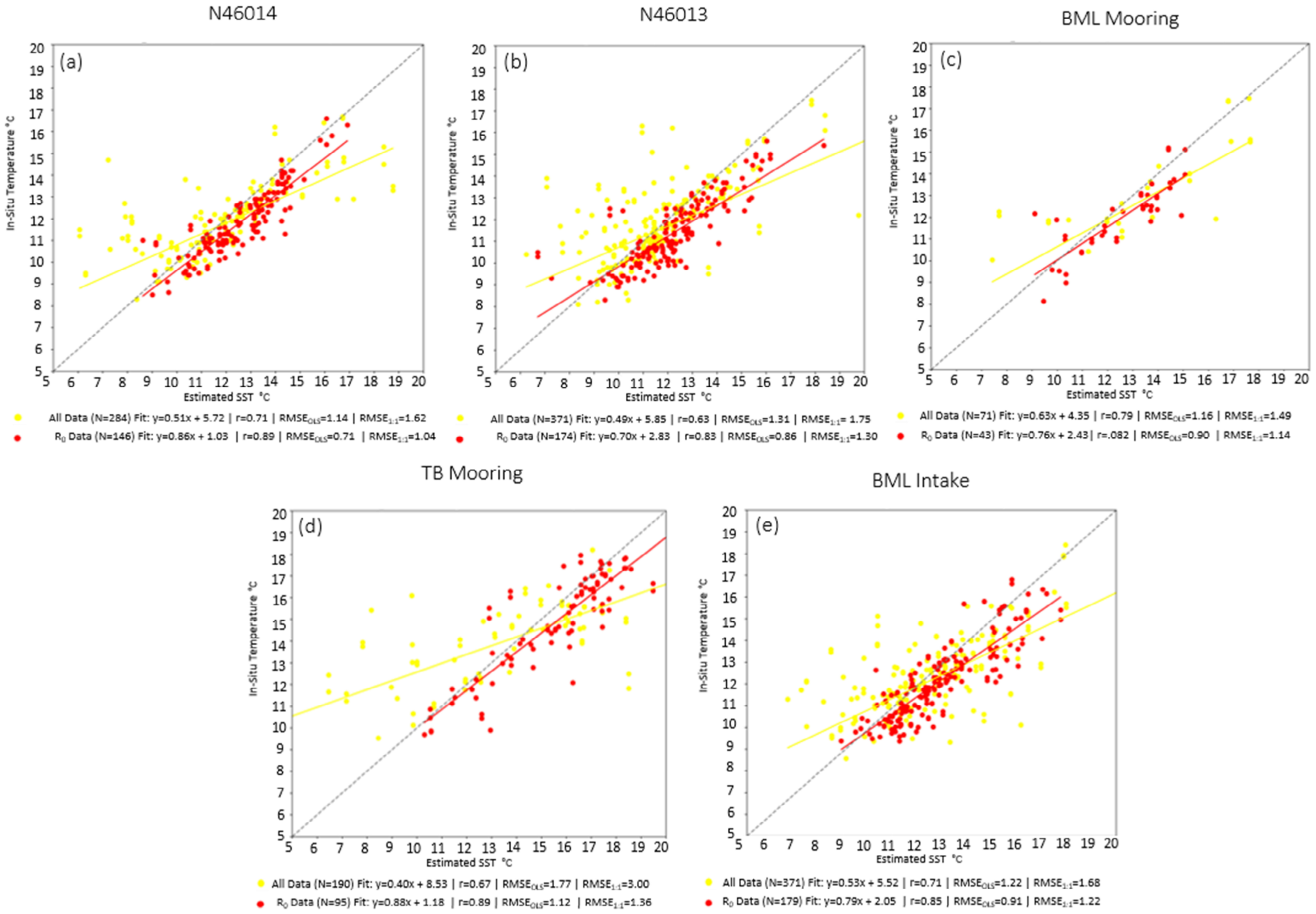

Figure 6. SST estimates from per-image-calibrated Landsat data plotted against water temperature from in situ sensors: (**a**) N46014, (**b**) N46013, (**c**) BML Mooring, (**d**) TB Mooring, and (**e**) BML Intake. Yellow data and trendline are for the All data dataset and red data and trendline are for R_0 data.

Seen in Figure 6, per-image calibration with the "selected" R_0 group notably improved accuracy. Correlation was highest at N46014 and TB Mooring (r = 0.89), with the lowest error metrics at N46014 ($RMSE_{OLS}$ = 0.71 °C; $RMSE_{1:1}$ = 1.04 °C). The Landsat-calibrated SST for these selected images was consistently more accurate than B_t or M_{SST} across sites, with both $RMSE_{OLS}$ and $RMSE_{1:1}$ at least 0.4 °C lower except at BML Mooring, where differences were minimal.

The performance of SST estimates based on the "generalized calibration" equation was considerably superior (Figure 7, Table 1) Within the "all data" dataset, SST estimates are best at BML Mooring, where the correlation is strongest (r = 0.92) and error metrics are lowest ($RMSE_{OLS}$ = 0.76 °C; $RMSE_{1:1}$ = 0.95 °C). N46013 had the lowest correlation (r = 0.73), and TB Mooring had the highest error ($RMSE_{OLS}$ = 1.25 °C; $RMSE_{1:1}$ = 1.56 °C). The performance across all metrics outperforms that from M_{SST} and Bt at all sites except for $RMSE_{OLS}$ and r at BML Intake, where MODIS estimates are slightly better when using "all data".

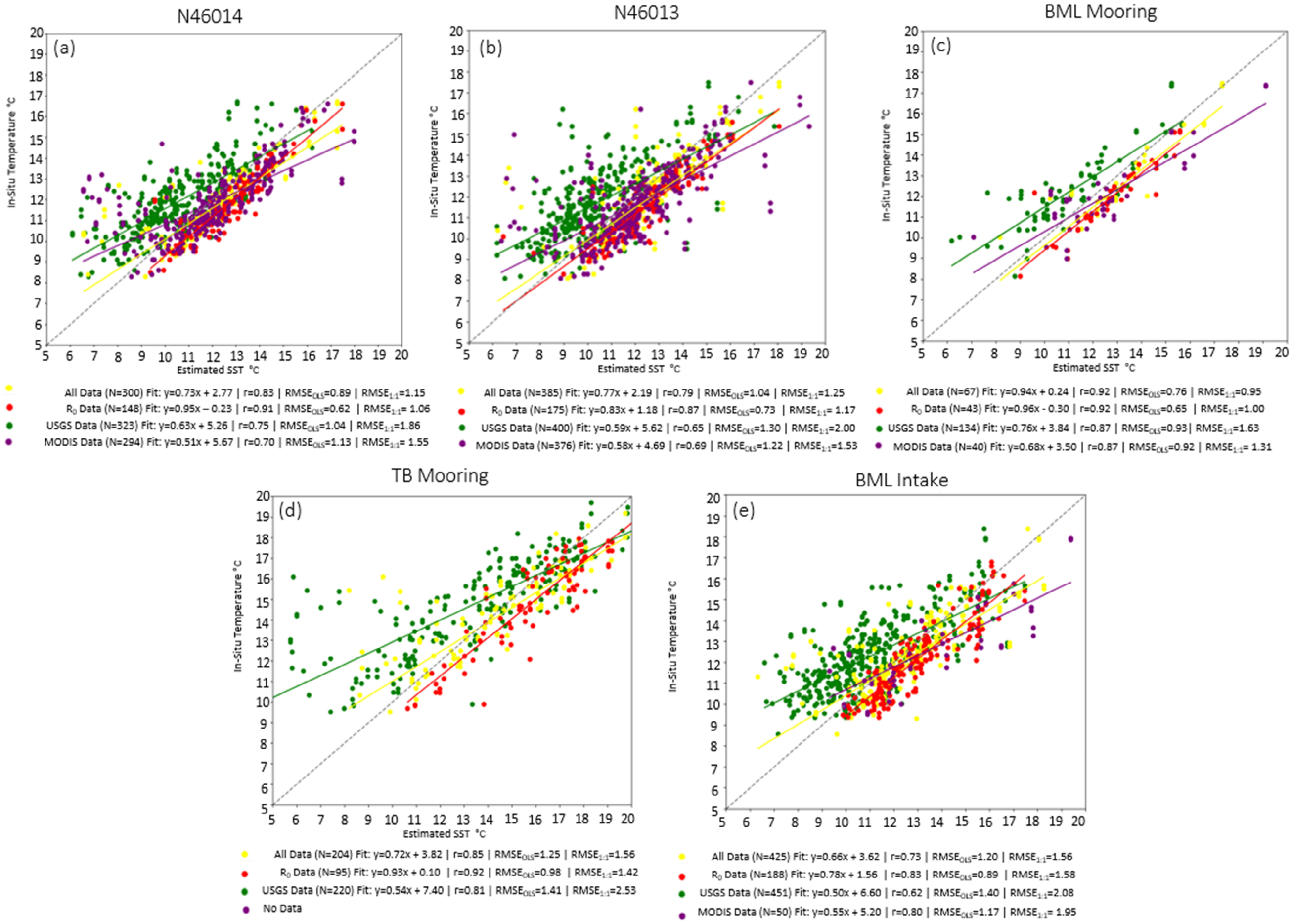

Figure 7. SST estimates from generalized-equation-calibrated Landsat data plotted against water temperature measured by in situ sensors: (**a**) N46014, (**b**) N46013, (**c**) BML Mooring, (**d**) TB Mooring, and (**e**) BML Intake. Yellow data and trendline are for the All data dataset, red data and trendline are for R_0 data, green data and trend line are for USGS B_t data and purple is MODIS SST data.

As expected, performance is significantly stronger within the "selected" R_0 group. Correlation is strongest at BML Mooring, TB Mooring, and N46014 sites (respectively, r = 0.92, 0.92, 0.91). The error from the OLS line is lowest at N46014 ($RMSE_{OLS}$ = 0.62 °C) and BML Mooring ($RMSE_{OLS}$ = 0.65 °C). The error relative to the 1:1 line is lowest at BML Mooring ($RMSE_{1:1}$ = 1.00). Despite slightly weaker performance at BML Intake (r = 0.83; $RMSE_{1:1}$ = 1.58 °C) and errors at TB Mooring ($RMSE_{OLS}$ = 0.98 °C), SST estimates from the generalized calibration remained more accurate than M_{SST} or Bt at all sites (Figure 7 and Table 1).

Figure 8 shows the differences between SST estimated from the "generalized calibration" equation and in situ sensor-measured data for "all data" aggregated by month. Across all buoys and months, SST is higher than T_{insitu}. Within the "all data" dataset, this difference is greatest within the summer months from June to August, where median differences are ~1.5 °C on average and smallest in December and January.

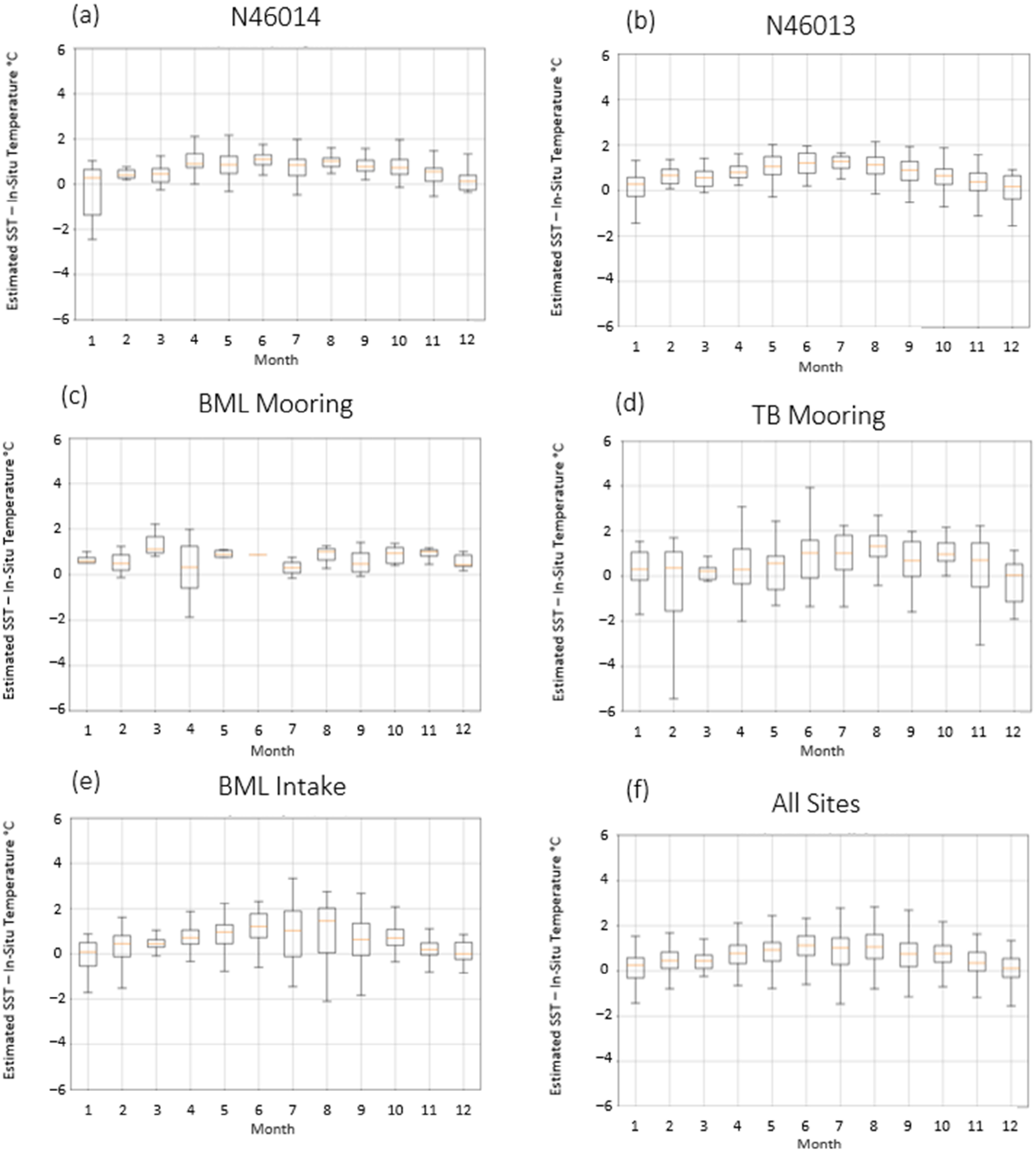

Figure 8. Monthly box and whisker plots of difference between estimated SST and in situ measurements across "all data". Box margins are lower 25th percentile of difference (lower bound) and 75th percentile of difference (upper bound). Orange line in box is monthly median. Whiskers show minimum and maximum difference values. (**a**) N46014, (**b**) N46013, (**c**) BML Mooring, (**d**) TB Mooring, (**e**) BML Intake, and (**f**) all buoy locations combined.

4. Discussion

4.1. Image Calibration

We have developed and assessed a methodology for calibrating Landsat brightness data using coincidental MODIS data. This allows for the production of fine-scale SST imagery invaluable for resolving patterns in the nearshore ocean. By comparing SST estimates produced through our generalized-equation methodology with coincident in situ sensor data, we show markedly superior performance versus the standard USGS Level 2 Landsat B_t data, as well as the standard MODIS SST data. This methodology not only enhances the overall estimation of SST but also allows for the semi-objective selection of an image dataset.

Per-image calibration (Figure 6), when applied to our minimally filtered "all" dataset, showed mixed reliability, with $RMSE_{OLS}$ similar to land-calibrated B_t data found in Figure 7. However, the $RMSE_{1:1}$ error from this dataset was generally lower than in the B_t data (e.g., BML Intake was 0.40 °C lower). These results suggest that unsupervised per-image calibration (as in past studies) may only conditionally yield a lower error than using B_t data. In environments close to shore, such as BML Intake, per-image calibration provided a -0.27 °C lower error than M_{SST}, displaying its value for areas where MODIS data are unavailable, such as at TB Mooring. The performance of per-image calibration is better when applied to a tighter selection of images ("selected" data in the R_0 grouping). This approach exhibits increased correlation and reduced error relative to both USGS Level 2 B_t data and M_{SST} (Figure 6), particularly at sites closest to the shore. The selection of images based on calibration not only proved efficient for isolating a "selected" R_0 dataset—a task traditionally performed manually and often arduous—but also facilitated the development of a generalized equation.

Across all metrics and sites, SST estimates from the generalized equation demonstrated superior accuracy. SST estimates from both datasets significantly outperformed the B_t and M_{SST} data, even at sites where per-image calibration had struggled.

In SST calibrated with the per-image approach, the "selected" data had an average correlation r = 0.154 higher than the "all data", a reduction in $RMSE_{OLS}$ of -0.31 °C, and a reduction in $RMSE_{1:1}$ of -0.46 °C. However, in SST calibrated with the generalized equation step, the "selected" data correlation was only r = 0.07 higher than the "all data", the reduction in $RMSE_{OLS}$ was -0.25 °C, and the reduction in $RMSE_{1:1}$ was only -0.048 °C. This consistency affirms that selective image calibration is largely unnecessary once the generalized equation is in place, thereby expanding the dataset and allowing for reliable SST estimation over more extended time frames and diverse coastal environments.

To explore whether Landsat data can be calibrated independent of MODIS data by using this generalized equation, we apply it to Landsat B_T data before the launch of the MODIS Terra satellite (Landsat 5 data from 1984 to 2000) and after its reliable data quality window (Landsat 8 and 9 data after 2023). Validations based on in situ sensor data (Figure 9) show comparable performance (correlation, $RMSE_{1:1}$, and $RMSE_{OLS}$) with validations from the 2000–2023 dataset. While historical Landsat 5 data appear to exhibit a better fit with in situ measurements, the recent data have a significantly smaller sample size, inadequate for the analysis of methodological success. Given the excellent performance of the generalized equation on independent data, it is likely that this equation will perform well at sites elsewhere that are comparable to those in WRS tile path 45 row 33 (e.g., other coastal upwelling regions with similar stratification patterns).

The superior performance of the generalized equation is expected, as this composite approach based on "selected" image pairs excludes any misleading image pairs that may retain unresolved artifacts in either Landsat or MODIS data. Notably, the generalized equation approach removes the potential for error due to poor-quality MODIS data in coastal waters for specific overpass conditions. Nevertheless, there is a clear seasonal change in slope and intercept values (Figure 4c,d), which is largely due to a poorer determination of values in the winter months with higher cloud cover in this region.

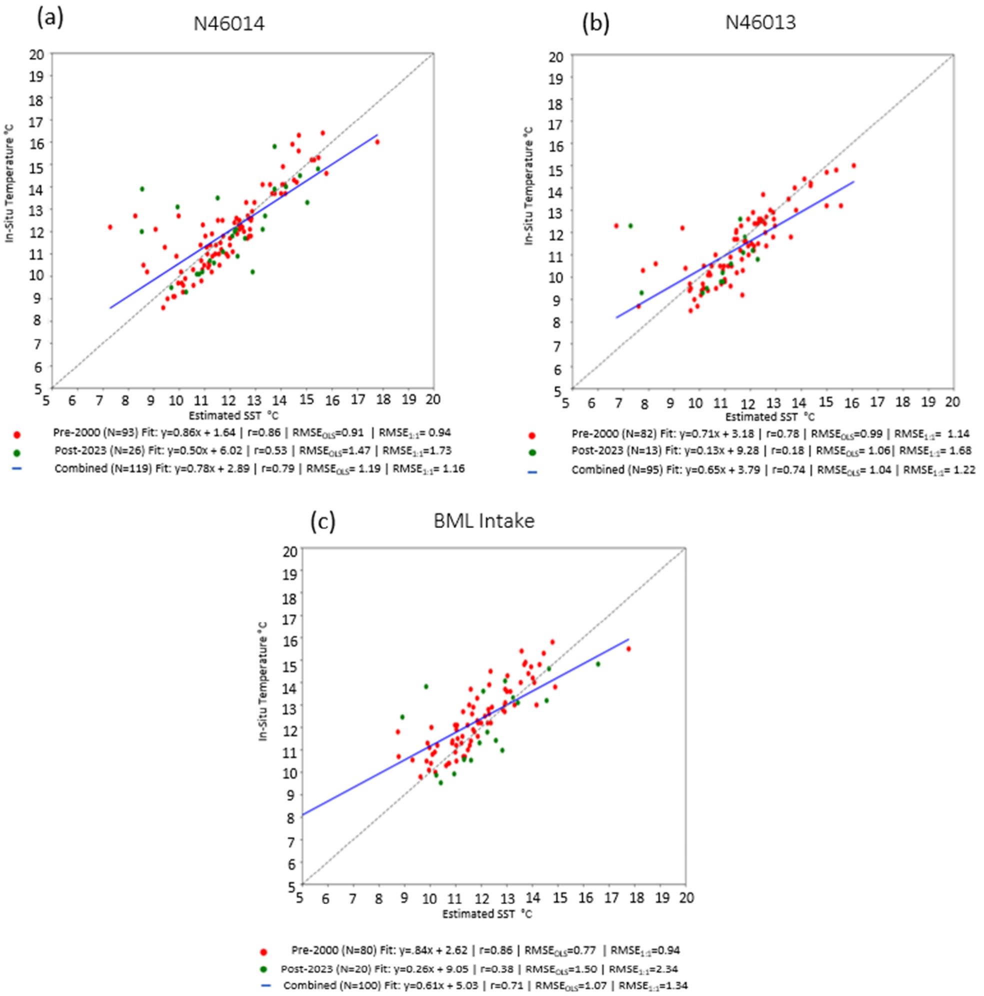

Figure 9. In situ sensor data on temperature at (**a**) N46014, (**b**) N46013, and BML Intake (**c**) plotted against SST data from general-equation calibration of Landsat B_t data before and after MODIS capture window. Green data points are data captured after 2023, and red data points are data captured prior to 2000. Blue trend line is OLS best-fit line for combination of those two data ranges.

4.2. Sources of Error

While overall accuracy between T_{insitu} and SST is high across sites and seasons, the agreement is not as strong at some sites (although still better than for SST from Landsat B_t or MODIS—see Table 1). This is expected, as the discrepancy between T_{insitu} and SST may be due to specifics of the in situ data at particular sites. While we compared satellite data with in situ data as an independent measure of how well the Landsat SST calibration works, it should be recognized that both measurements may differ from the true surface temperature of the ocean (i.e., skin temperature). Errors associated with satellite data are related to atmospheric effects and are well articulated in the remote sensing literature [49,50], including the effects of aerosols, fog, and wildfires [51]. Errors associated with in situ data are related to the vertical separation between the surface and the sensor in the presence of near-surface stratification [52,53].

Near-surface stratification develops in the presence of surface runoff or surface heating. In our study region, runoff effects occur in winter and are typically small [9]—while they could affect near-coastal locations like the Bodega Head or Tomales Bay sites, surface heating is weak in winter. In summer, there is a persistently positive heat flux associated with the low surface temperatures of upwelled water [54]. As described previously, thermal stratification may develop near the surface during calm periods, above the depth of near-surface sensors [52,53]. However, on windy days, near-surface waters are mixed and isothermal to depths below near-surface sensors; prior studies have identified wind speeds of 6 m/s as a threshold for well-mixed near-surface conditions [55,56]; this value is often exceeded in coastal waters off northern California [36,57]. The discrepancy between skin and bulk temperatures due to surface heating is expected to yield positive errors ($SST > T_{insitu}$), as seen in Figure 7. For sites with the best agreements between T_{insitu} and SST (e.g., BML Mooring), the offset between regression line values and 1:1 line values is about 0.5 °C in the center of the data range. Similar values have been seen in prior studies of the discrepancy between skin and bulk temperatures [52,58], suggesting that this half-degree positive bias in SST values is primarily due to near-surface stratification. Furthermore, the slopes of the regression lines are less than the slope of the 1:1 line, accounting for a smaller offset at lower temperatures, consistent with the expectation that the offset tends toward zero on windy days as cold water is well correlated with strong winds in this and other upwelling regions [37,54]. In addition to this persistent bias (offset), other transient effects may contribute to differences between skin and bulk temperatures (e.g., internal wave runup; diurnal warming) and combine with atmospheric effects to account for the noise in both measurements, which is indexed by RMS errors. Without a high-resolution field experiment, it is difficult to attribute error more specifically.

Given that the offset from the 1:1 line is explained by differences between skin and bulk water temperatures, an appropriate measure of the performance of Landsat SST as a measure of skin temperature is the RMS error relative to the linear regression line. Thus, we estimate the uncertainty in the method as 0.62 °C from calculating the RMS error using the best data at the best site (R_0 data at N46014, Figure 7). This is supported by low RMS errors elsewhere, with less than 1.0 °C for R_0 data at all sites and less than 0.73 °C at all mooring sites.

In general, the high performance at both offshore and nearshore mooring sites (N46013, N46014, BML Mooring) highlights the skill of our SST calibration methodology in coastal waters. Correlations for selected R_0 data at mooring sites vary between 0.87 and 0.92, with RMS errors between 0.62 and 0.73 °C (Table 1; Figure 7). The lowest correlation and highest error are found at BML Intake, which is a sensor on an intake pipe at a fixed depth that does not adjust with tidal level. Furthermore, the pipe is deeper than buoy sensors, varying between 2.5 and 4.5 m below the surface within a cove that is partially sheltered from waves and winds. The sensor temperature at this site may differ significantly from the true surface (skin) temperature [48,56]. In other words, our calibrated SST may still perform well here. The second-highest error is found at TB Mooring in Tomales Bay, which is a low-inflow estuary. Although this buoy-mounted sensor is shallow (~1 m below surface), the Bay can exhibit stratification due to cold-water intrusions in summer and low-salinity runoff in winter [11,59] and again, the poorer agreement between SST and in situ data may be unrelated to the performance of the calibrated SST in representing the true surface (skin) temperature. At offshore mooring sites N46013 and N46014, near-surface stratification likely accounts for an increased positive difference in summer months (maximum in June–August), when surface heating creates near-surface stratification in cold upwelled waters (Figure 8) [30,37,60].

4.3. Observation and Use Cases

High-resolution SST data allow for the observation of small-scale nearshore processes that are too fine for detection with moderate-resolution data products like GOES or MODIS. This enhancement enables the study of phenomena such as rip currents and their impact on temperature patterns in the nearshore. Moreover, it facilitates the observation of various non-turbid dynamics, irrespective of their size, which are typically not observable in visual–optical/color satellite radiances. Examples include clear river plumes, tidal outflows from bays and estuaries, and fine-scale eddies.

Figure 10 showcases these features. Fine-scale cold features align with the shapes and locations of small turbid rip currents visible in high-resolution true-color imagery along the Pt. Reyes Seashore (Figure 10d). The calibrated high-resolution SST in this figure also illuminates the shapes and extents of non-turbid mixing processes, manifesting as small clear river plumes (Figure 10b) and tidal bay outflows (Figure 10c). While these features may be identified in uncalibrated brightness values, calibration allows for the quantification of the temperatures of these features and provides a clearer understanding of the thermal differences between these features and ambient coastal waters, which could not be verified with uncalibrated brightness temperature values.

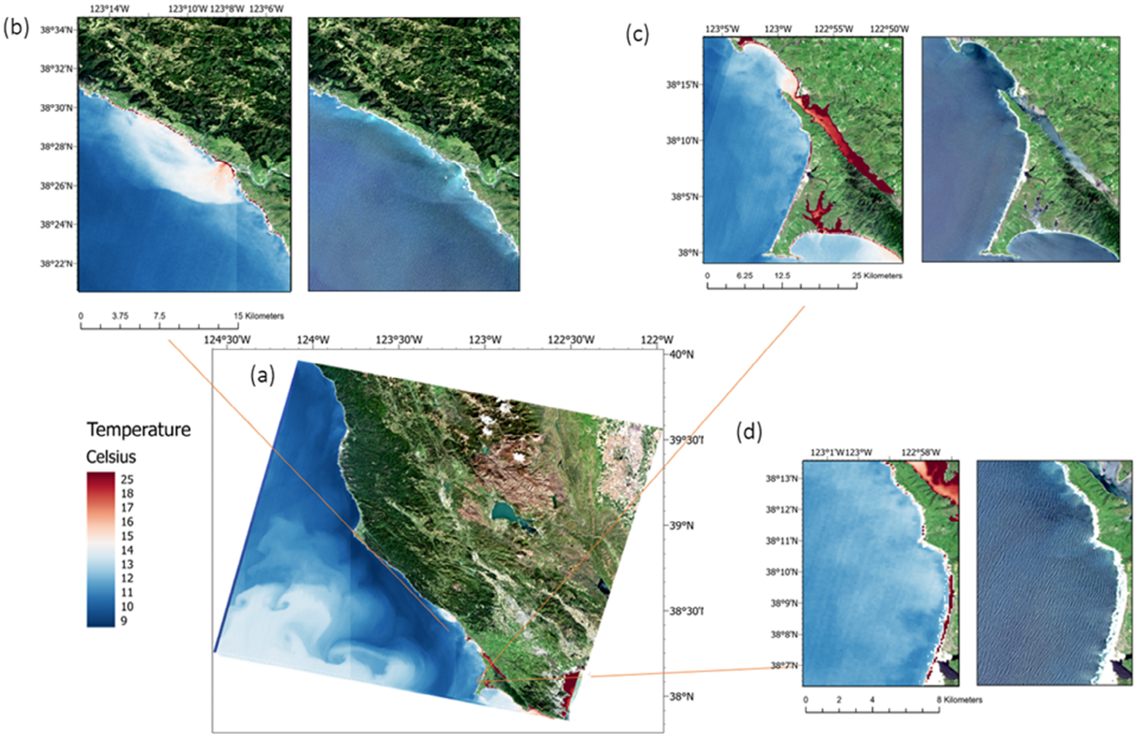

Figure 10. Mapped temperature from 25 April 2019 vs. true-color values at zoomed-in sites. Color scale adjusted to highlight all temperature features. (**a**) Entire calibrated SST image. (**b**) Zoomed-in calibrated SST (left) and true-color imagery (right) directly west of the Russian River estuary. (**c**) Zoomed-in calibrated SST (left) and true-color imagery (right) north of the Pt. Reyes National Seashore and south of Bodega Bay. (**d**) Zoomed-in calibrated SST (left) and true-color imagery (right) of the north headland of Point Reyes national seashore.

The capability to sample SST with high spatial resolution enhances the ability to monitor regions where regular in situ data collection is challenging, such as immediate and often rocky nearshore areas. This facilitates novel observational studies and research projects. For instance, an application of this methodology is the investigation of disparities between nearshore temperatures and ambient coastal waters, including effects of the coastal boundary layer [14] and the surf zone [61]. For example, plots of high-resolution SST for a cross-shore transect off Manchester Bay show the possibility that waters within a kilometer of the shore are 1–2 °C warmer or cooler than those offshore (Figure 11). Interestingly, even though the observations were made at the same location and during the same season, the temperature gradients along this transect showed varying trends—warming, cooling, or displaying a parabolic shape with increasing distance from the shore.

Recognizing that these high-resolution SST data are available as far back as 1984, we can determine fine-scale climatology across an extensive spatial area. For example, the mean SST map in Figure 12 shows a familiar pattern with the coldest waters at the Point Arena upwelling center [36,37] but also fine-scale nearshore zones off the Russian River, in Bodega Bay, and along the north shore of Point Reyes that are a few degrees warmer than upwelled waters further offshore. Narrower nearshore features are also evident off other north-facing beaches such as Ten Mile, Manchester, and Salmon Creek. A second upwelling maximum is apparent near Fort Bragg.

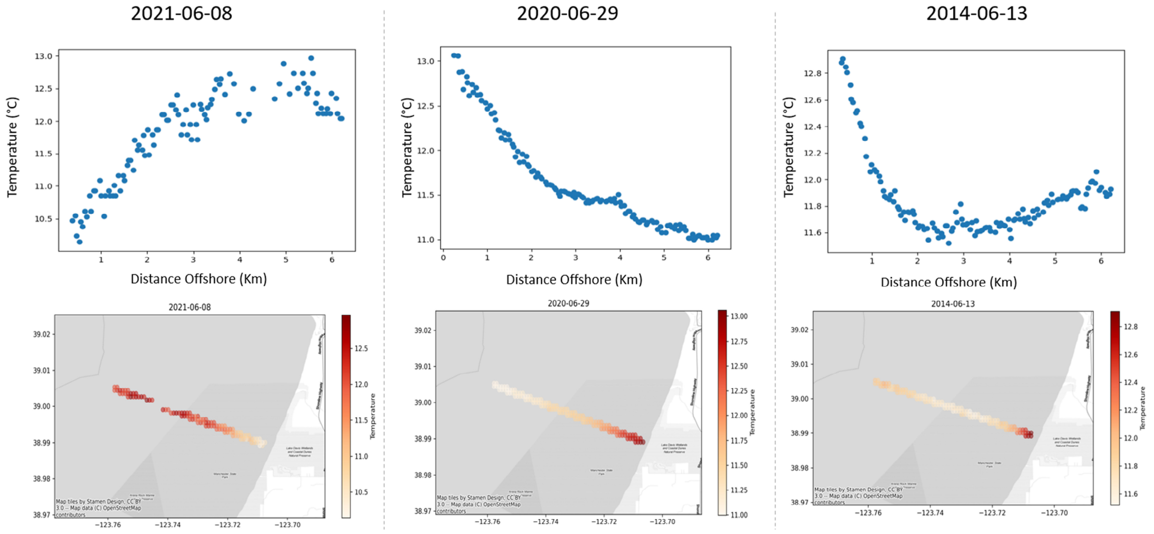

Figure 11. Cross-shore temperature profiles from a transect at Manchester Beach, CA, extending 6.5 km offshore from per-image calibrated images. (**Top**) Plots of temperature (y-axis) vs. distance (x-axis). (**Bottom**) Mapped temperature values from dates respective to plots in the same column.

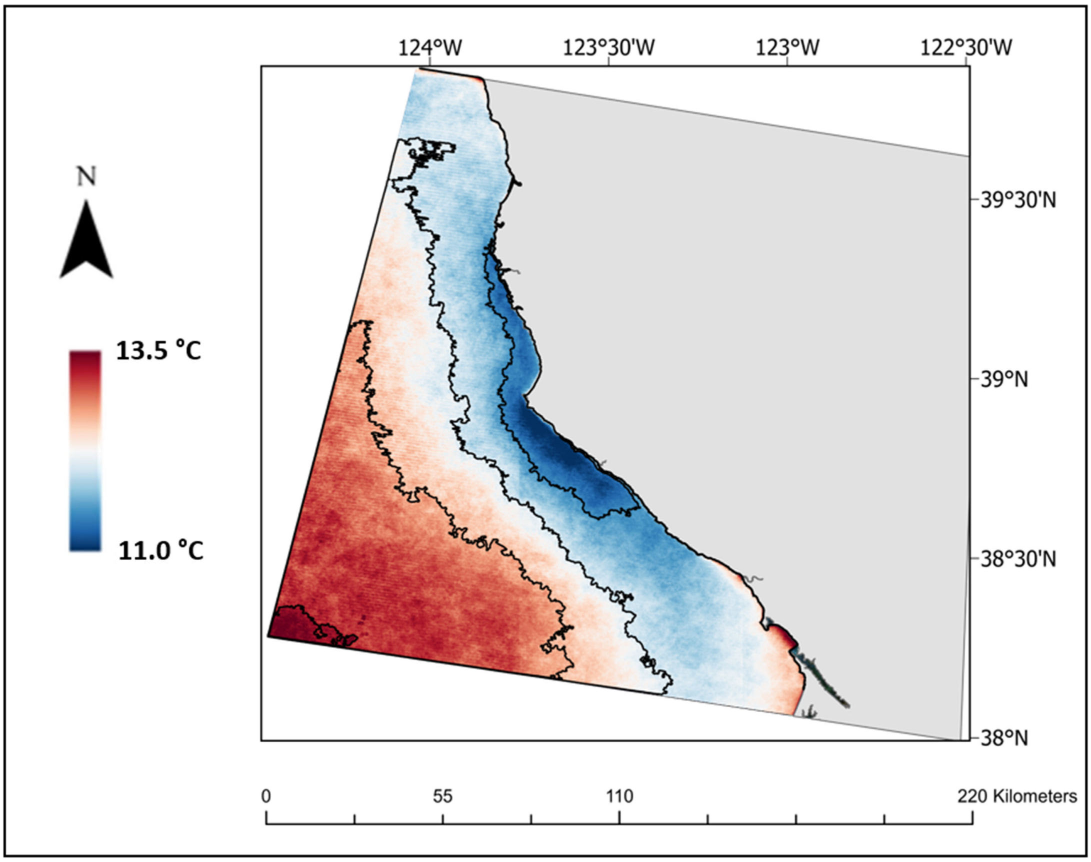

Figure 12. Average SST at each pixel position in calibrated Landsat data from 1983 to 2024 in degrees Celsius calibrated using generalized equation. Isothermal contours are shown for 11.5°, 12.0°, 12.5°, and 13.0 °C.

5. Conclusions

In our research, we develop, validate, and apply a two-step methodology for deriving nearshore ocean water surface temperature from Landsat land brightness temperatures in WRS tile path 45 row 33 using associated MODIS Terra SST data. By deriving calibration constants from relationships between coincident MODIS Terra and Landsat data, we can calibrate data prior to, during, and after the operational extent of reliable MODIS Terra SST data. For validation, we tested our calibrated data against in situ temperature measurements collected from sensors at various distances offshore within the study area and compared these validations against those with values from uncalibrated USGS Landsat land brightness temperatures and coincident MODIS SSTs. We find superior accuracy compared with the off-the-shelf USGS product and even with coincident MODIS SST data. For a minimally filtered dataset (n = 557 images), the RMSE against the OLS line ranges between 0.76 and 1.20 °C, the RMSE against the 1:1 line ranges between 0.95 and 1.56 °C, and correlation coefficients range from r = 0.73 to 0.92. These metrics are further enhanced when looking at comparisons within our R_0 dataset (n = 229), which consists of optimal images whose selection was enabled by our methodology. This dataset has an RMSE against the OLS line ranging between 0.62 and 0.98 °C, an RMSE against the 1:1 line ranging between 1.00 and 1.58 °C, and correlation coefficients ranging from r = 0.83 to 0.92. Furthermore, it appears that the larger errors in validation may be related to seasonal impacts, such as near-surface stratification, so that the smallest errors are likely most representative of the skill of this calibrated Landsat data in representing true surface temperatures—this error is between 0.62 and 0.73 °C.

The first step of our method enhances existing techniques for calibrating single-image Landsat brightness temperature to SST using coincident MODIS data and extends its application across hundreds of images rather than isolated dates. The second step develops a generalized equation based on constants derived from median statistics of the best-fit correlation equations from data derived from and selected with the first-step methodology. This calibration exhibits uniformly enhanced data correlation across the dataset with in situ temperature data both nearshore and offshore. This methodology's strength lies in its ability to transcend inaccuracies potentially introduced by artifacts such as undetected clouds and shadows, which can adversely affect per-image calibrations. The resulting data quality, closely aligned with in situ measurements, underscores the value of a generalized approach in achieving more consistent and accurate SST estimations. The success in applying the generalized calibration to historical satellite data not only validates the robustness and utility of the methodology but also broadens the temporal scope of fine-scale SST analyses, including long-term climatological assessments.

The goal of this paper is to provide an easily applied and replicable methodology for optimizing SST data for nearshore observation. Future work could test these calibration constants in other regions to assess the broader applicability of this methodology. This would help validate the robustness of the approach and extend its utility. It is expected that this calibration will perform well in coastal areas with similar oceanographic characteristics, such as upwelling regions along western continental boundaries. Furthermore, an investigation of the impacts of stratification on the calibration methodology could help refine and enhance future efforts in deriving high-resolution SST data from satellite imagery. Here, we show the promise of fine-scale SST data for questions that cannot be addressed with coarser moderate-resolution SST data. Specifically, we are motivated by the prospect that these high-resolution SST data will provide unique perspectives on nearshore processes, with significant new insights related to nearshore water quality and ecosystems.

Author Contributions: W.H.S.: writing—original draft, visualization, validation, methodology, investigation, formal analysis, data curation, conceptualization. J.L.L.: writing—review and editing, investigation, funding acquisition, conceptualization. All authors have read and agreed to the published version of the manuscript.

Funding: We are grateful for funding from the State of California (CA Ocean Protection Council grant) and the National Science Foundation (DISES grant #2108002).

Data Availability Statement: All data in this study are derived from public domain resources noted in the writing. For any further information, please contact the corresponding author.

Acknowledgments: Gonzalo Saldías and Yufang Jin are thanked for their feedback contributing to the methodology within the manuscript.

Conflicts of Interest: The authors declare that they have no known competing financial interests or personal relationships that could have appeared to influence the work reported in this paper.

References

1. Pauly, D.; Christensen, V. Primary Production required to sustain global fisheries. *Nature* **1995**, *374*, 255–257. [CrossRef]
2. Muller-Karger, F.E.; Hestir, E.; Ade, C.; Turpie, K.; Roberts, D.A.; Siegel, D.; Miller, R.J.; Humm, D.; Izenberg, N.; Keller, M.; et al. Satellite sensor requirements for monitoring essential biodiversity variables of coastal ecosystems. *Ecol. Appl.* **2018**, *28*, 749–760. [CrossRef] [PubMed]
3. Feng, L.; Hu, C. Land adjacency effects on MODIS A qua top-of-atmosphere radiance in the shortwave infrared: Statistical assessment and correction. *J. Geophys. Res. Ocean.* **2017**, *122*, 4802–4818. [CrossRef]
4. Ding, H.; Elmore, A.J. Spatio-temporal patterns in water surface temperature from Landsat time series data in the Chesapeake Bay, USA. *Remote Sens. Environ.* **2015**, *168*, 335–348. [CrossRef]
5. Brewin, R.J.W.; Smale, D.A.; Moore, P.J.; Dall'olmo, G.; Miller, P.I.; Taylor, B.H.; Smyth, T.J.; Fishwick, J.R.; Yang, M. Evaluating operational AVHRR sea surface temperature data at the coastline using benthic temperature loggers. *Remote Sens.* **2018**, *10*, 925. [CrossRef]
6. MacMahan, J.H.; Thornton, E.B.; Reniers, A.J. Rip current review. *Coast. Eng.* **2006**, *53*, 191–208. [CrossRef]
7. Largier, J.L. Rip currents and the influence of morphology on wave-driven cross-shore circulation. In *Reference Module in Earth Systems and Environmental Sciences*; Elsevier: Amsterdam, The Netherlands, 2022; pp. 100–121.
8. Horner-Devine, A.R.; Hetland, R.D.; MacDonald, D.G. Mixing and transport in coastal river plumes. *Annu. Rev. Fluid Mech.* **2015**, *47*, 569–594. [CrossRef]
9. Basdurak, N.B.; Largier, J.L.; Nidzieko, N.J. Modeling the dynamics of small-scale river and creek plumes in tidal waters. *J. Geophys. Res. Oceans* **2020**, *125*, e2019JC015737. [CrossRef]
10. Speiser, W.H.; Largier, J.L. Long-term observations of the turbid outflow plume from the Russian River, California. *Estuar. Coast. Shelf Sci.* **2024**, *309*, 108942. [CrossRef]
11. Chadwick, D.B.; Largier, J.L.; Cheng, R.T. The role of thermal stratification in tidal exchange at the mouth of San Diego Bay. *Buoyancy Eff. Coast. Estuar. Dyn.* **1996**, *53*, 155–174.
12. Wolanski, E.; Elliott, M. *Estuarine Ecohydrology: An Introduction*; Elsevier: Amsterdam, The Netherlands, 2015.
13. Lamb, K.G. Internal wave breaking and dissipation mechanisms on the continental slope/shelf. *Annu. Rev. Fluid Mech.* **2014**, *46*, 231–254. [CrossRef]
14. Nickols, K.J.; Gaylord, B.; Largier, J.L. The coastal boundary layer: Predictable current structure decreases alongshore transport and alters scales of dispersal. *Mar. Ecol. Prog. Ser.* **2012**, *464*, 17–35. [CrossRef]
15. Lentz, S.J.; Fewings, M.R. The wind-and wave-driven inner-shelf circulation. *Annu. Rev. Mar. Sci.* **2012**, *4*, 317–343. [CrossRef] [PubMed]
16. Gough, M.K.; Freismuth, T.M.; MacMahan, J.H.; Colosi, J.A.; Suanda, S.H.; Kumar, N. Heating of the midshelf and inner shelf by warm internal tidal bores. *J. Phys. Oceanogr.* **2020**, *50*, 2609–2620. [CrossRef]
17. Largier, J.L. Upwelling bays: How coastal upwelling controls circulation, habitat, and productivity in bays. *Annu. Rev. Mar. Sci.* **2020**, *12*, 415–447. [CrossRef]
18. Albanai, J.A.; Abdelfatah, S.A. Accuracy assessment for Landsat 8 thermal bands in measuring sea surface temperature over Kuwait and North West Arabian Gulf. *Kuwait J. Sci.* **2022**, *49*, 1–13. [CrossRef]
19. Choung, Y.J.; Kim, J.M. Relationship between the In-situ-measured Sea Surface Temperatures and the Landsat-derived Brightness Temperatures: A Case Study in the West Coast of South Korea. *J. Coast. Res.* **2019**, *91*, 336–340. [CrossRef]
20. Klein, K.P.; Lantuit, H.; Heim, B.; Fell, F.; Doxaran, D.; Irrgang, A.M. Long-term high-resolution sediment and sea surface temperature spatial patterns in Arctic nearshore waters retrieved using 30-year landsat archive imagery. *Remote Sens.* **2019**, *11*, 2791. [CrossRef]
21. Tavora, J.; Jiang, B.; Kiffney, T.; Bourdin, G.; Gray, P.C.; Carvalho, L.S.; Hesketh, G.; Schild, K.M.; Souza, L.F.; Brady, D.C.; et al. Recipes for the derivation of water quality parameters using the high-spatial-resolution data from sensors on board sentinel-2A, sentinel-2B, Landsat-5, Landsat-7, Landsat-8, and Landsat-9 satellites. *J. Remote Sens.* **2023**, *3*, 0049. [CrossRef]
22. Vanhellemont, Q. Automated water surface temperature retrieval from Landsat 8/TIRS. *Remote Sens. Environ.* **2020**, *237*, 111518. [CrossRef]
23. Wloczyk, C.; Richter, R.; Borg, E.; Neubert, W. Sea and lake surface temperature retrieval from Landsat thermal data in Northern Germany. *Int. J. Remote Sens.* **2006**, *27*, 2489–2502. [CrossRef]

24. Jang, J.; Park, K.A. High-resolution sea surface temperature retrieval from Landsat 8 OLI/TIRS data at coastal regions. *Remote Sens.* **2019**, *11*, 2687. [CrossRef]
25. Syariz, M.A.; Jaelani, L.M.; Subehi, L.; Pamungkas, A.; Koenhardono, E.S.; Sulisetyono, A. Retrieval of sea surface temperature over Poteran Island water of Indonesia with Landsat 8 TIRS image: A preliminary algorithm. *Int. Arch. Photogramm. Remote Sens. Spat. Inf. Sci.* **2015**, *40*, 87–90. [CrossRef]
26. Bocharov, A.V.; Kostianoy, A.G.; Lebedev, S.A. Assessment of the accuracy of determining the Caspian Sea surface temperature by Landsat-5,-7 satellites based on the measurements of drifters. *Ecol. Montenegrina* **2024**, *76*, 87. [CrossRef]
27. Wachmann, A.; Starko, S.; Neufeld, C.J.; Costa, M. Validating Landsat Analysis Ready Data for Nearshore Sea Surface Temperature Monitoring in the Northeast Pacific. *Remote Sens.* **2024**, *16*, 920. [CrossRef]
28. Kuroda, H.; Toya, Y. High-resolution sea surface temperatures derived from Landsat 8: A study of submesoscale frontal structures on the Pacific shelf off the Hokkaido coast, Japan. *Remote Sens.* **2020**, *12*, 3326. [CrossRef]
29. Thomas, A.; Byrne, D.; Weatherbee, R. Coastal sea surface temperature variability from Landsat infrared data. *Remote Sens. Environ.* **2002**, *81*, 262–272. [CrossRef]
30. Fisher, J.I.; Mustard, J.F. High spatial resolution sea surface climatology from Landsat thermal infrared data. *Remote Sens. Environ.* **2004**, *90*, 293–307. [CrossRef]
31. Snyder, J.; Boss, E.; Weatherbee, R.; Thomas, A.C.; Brady, D.; Newell, C. Oyster aquaculture site selection using Landsat 8-derived sea surface temperature, turbidity, and chlorophyll a. *Front. Mar. Sci.* **2017**, *4*, 190. [CrossRef]
32. Snyder, J.N.; Bell, T.W.; Siegel, D.A.; Nidzieko, N.J.; Cavanaugh, K.C. Sea surface temperature imagery elucidates spatiotemporal nutrient patterns for offshore kelp aquaculture siting in the southern california bight. *Front. Mar. Sci.* **2020**, *7*, 22. [CrossRef]
33. Fu, J.; Chen, C.; Guo, B.; Chu, Y.; Zheng, H. A split-window method to retrieving sea surface temperature from Landsat 8 thermal infrared remote sensing data in offshore waters. *Estuar. Coast. Shelf Sci.* **2020**, *236*, 106626. [CrossRef]
34. Twedt, K.; Xiong, X.; Geng, X.; Wilson, T.; Mu, Q. Impact of satellite orbit drift on MODIS Earth scene observations used in calibration of the reflective solar bands. In *Earth Observing Systems XXVIII*; SPIE: Bellingham, DC, USA, 2023; Volume 12685, pp. 158–167.
35. Behrens, D.K.; Bombardelli, F.A.; Largier, J.L.; Twohy, E. Episodic closure of the tidal inlet at the mouth of the Russian River—A small bar-built estuary in California. *Geomorphology* **2013**, *189*, 66–80. [CrossRef]
36. Garcia-Reyes, M.; Largier, J.L. Seasonality of coastal upwelling off central and northern California: New insights, including temporal and spatial variability. *J. Geophys. Res. Oceans* **2012**, *117*, C03028. [CrossRef]
37. Largier, J.L.; Magnell, B.A.; Winant, C.D. Subtidal circulation over the northern California shelf. *J. Geophys. Res. Oceans* **1993**, *98*, 18147–18179. [CrossRef]
38. Halle, C.M.; Largier, J.L. Surface circulation downstream of the Point Arena upwelling center. *Cont. Shelf Res.* **2011**, *31*, 1260–1272. [CrossRef]
39. Gorelick, N.; Hancher, M.; Dixon, M.; Ilyushchenko, S.; Thau, D.; Moore, R. Google Earth Engine: Planetary-scale geospatial analysis for everyone. *Remote Sens. Environ.* **2017**, *202*, 18–27. [CrossRef]
40. Chander, G.; Markham, B.L.; Helder, D.L. Summary of current radiometric calibration coefficients for Landsat MSS, TM, ETM+, and EO-1 ALI sensors. *Remote Sens. Environ.* **2009**, *113*, 893–903. [CrossRef]
41. USGS, Landsat. *Landsat 8–9 Calibration and Validation (Cal/Val) Algorithm Description Document (ADD)*; United States Geological Society: Sioux Falls, SD, USA, 2021.
42. Foga, S.; Scaramuzza, P.L.; Guo, S.; Zhu, Z.; Dilley, R.D.; Beckmann, T.; Schmidt, G.L.; Dwyer, J.L.; Hughes, M.J.; Laue, B. Cloud detection algorithm comparison and validation for operational Landsat data products. *Remote Sens. Environ.* **2017**, *194*, 379–390. [CrossRef]
43. Markham, B.L.; Storey, J.C.; Williams, D.L.; Irons, J.R. Landsat sensor performance: History and current status. *IEEE Trans. Geosci. Remote Sens.* **2004**, *42*, 2691–2694. [CrossRef]
44. Montanaro, M.; Gerace, A.; Lunsford, A.; Reuter, D. Stray light artifacts in imagery from the Landsat 8 Thermal Infrared Sensor. *Remote Sens.* **2014**, *6*, 10435–10456. [CrossRef]
45. Johnstone, J.A.; Dawson, T.E. Climatic context and ecological implications of summer fog decline in the coast redwood region. *Proc. Natl. Acad. Sci. USA* **2010**, *107*, 4533–4538. [CrossRef] [PubMed]
46. Torregrosa, A.; O'Brien, T.A.; Faloona, I.C. Coastal fog, climate change, and the environment. *Eos Trans. Am. Geophys. Union* **2014**, *95*, 473–474. [CrossRef]
47. Zhang, H.K.; Roy, D.P. Landsat 5 Thematic Mapper reflectance and NDVI 27-year time series inconsistencies due to satellite orbit change. *Remote Sens. Environ.* **2016**, *186*, 217–233. [CrossRef]
48. Minnett, P.J. The validation of sea surface temperature retrievals from spaceborne infrared radiometers. *Oceanogr. Space Revisit.* **2010**, *1*, 229–247.
49. Donlon, C.J.; Minnett, P.J.; Gentemann, C.; Nightingale, T.J.; Barton, I.J.; Ward, B.; Murray, M.J. Toward improved validation of satellite sea surface skin temperature measurements for climate research. *J. Clim.* **2002**, *15*, 353–369. [CrossRef]
50. Ghanea, M.; Moradi, M.; Kabiri, K.; Mehdinia, A. Investigation and validation of MODIS SST in the northern Persian Gulf. *Adv. Space Res.* **2016**, *57*, 127–136. [CrossRef]
51. Gutierrez, A.A.; Hantson, S.; Langenbrunner, B.; Chen, B.; Jin, Y.; Goulden, M.L.; Randerson, J.T. Wildfire response to changing daily temperature extremes in California's Sierra Nevada. *Sci. Adv.* **2021**, *7*, eabe6417. [CrossRef]

52. Murray, M.J.; Allen, M.R.; Merchant, C.J.; Harris, A.R.; Donlon, C.J. Direct observations of skin-bulk SST variability. *Geophys. Res. Lett.* **2000**, *27*, 1171–1174. [CrossRef]
53. Ward, B. Near-surface ocean temperature. *J. Geophys. Res. Oceans* **2006**, *111*, C02005. [CrossRef]
54. Lentz, S.J. A heat budget for the northern California shelf during CODE 2. *J. Geophys. Res. Ocean.* **1987**, *92*, 14491–14509. [CrossRef]
55. Donlon, C.J.; Nightingale, T.J.; Sheasby, T.; Turner, J.; Robinson, I.S.; Emergy, W.J. Implications of the oceanic thermal skin temperature deviation at high wind speed. *Geophys. Res. Lett.* **1999**, *26*, 2505–2508. [CrossRef]
56. Delgado, A.L.; Jamet, C.; Loisel, H.; Vantrepotte, V.; Perillo, G.M.; Piccolo, M.C. Evaluation of the MODIS-Aqua Sea-Surface Temperature product in the inner and mid-shelves of southwest Buenos Aires Province, Argentina. *Int. J. Remote Sens.* **2014**, *35*, 306–320. [CrossRef]
57. Dorman, C.E.; Winant, C.D. Buoy observations of the atmosphere along the west coast of the United States, 1981–1990. *J. Geophys. Res. Oceans* **1995**, *100*, 16029–16044. [CrossRef]
58. Schluessel, P.; Emery, W.J.; Grassl, H.; Mammen, T. On the bulk-skin temperature difference and its impact on satellite remote sensing of sea surface temperature. *J. Geophys. Res. Oceans* **1990**, *95*, 13341–13356. [CrossRef]
59. Largier, J.L.; Hollibaugh, J.T.; Smith, S.V. Seasonally hypersaline estuaries in Mediterranean-climate regions. *Estua. Coast. Shelf Sci.* **1997**, *45*, 789–797. [CrossRef]
60. Minnett, P.J.; Kilpatrick, K.A.; Podestá, G.P.; Evans, R.H.; Szczodrak, M.D.; Izaguirre, M.A.; Williams, E.J.; Walsh, S.; Reynolds, R.M.; Bailey, S.W.; et al. Skin sea-surface temperature from VIIRS on Suomi-NPP—NASA continuity retrievals. *Remote Sens.* **2020**, *12*, 3369. [CrossRef]
61. Smith, J.A.; Largier, J.L. Observations of nearshore circulation: Rip currents. *J. Geophys. Res. Oceans* **1995**, *100*, 10967–10975. [CrossRef]